# The Effect of Ultra-fine Alloying Elements on High-Temperature Strength and Fracture Toughness of Ti–Si–X and Ti–Cr–X Composites


**Bogdan Vasyliv, Z. A. Duriagina, V. V. Kulyk, V. I. Vavrukh, P. Ya. Lyutyy, T. M. Kovbasiuk, I. A. Lemishka, V. V. Vira, and M. Ya. Holovchuk**

**Abstract** In contrast to conventional titanium alloys, an operating temperature of which is limited by 300–500 °C, advanced Ti-based composites possess high fracture toughness and strength under bend and tensile loading in the temperature range of 20–650 °C. Owing to their high strength-to-weight ratio, these composites are promising for applications in components of modern engines (aircraft, rocket, and internal combustion ones) as well as other power equipment (compressors, gas turbines, fuel cells, etc.). However, there is a need to increase their operating temperature range up to 700–800 °C. In this work, mechanical behavior of Ti–Si–X composites (X = Al and/or Zr, Sn, C) has been studied. The content of alloying elements varied in a wide range (2–5 wt% Al, 2–5 wt% Zr, 1–5 wt% C). For comparison, mechanical behavior of Ti–Cr–X composite (X = Al and/or C) has been studied. The composites were

B. Vasyliv (✉)
Department of Hydrogen Technologies and Alternative Energy Materials, Karpenko Physico-Mechanical Institute of the NAS of Ukraine, 5 Naukova Str., Lviv 79060, Ukraine
e-mail: mechengin1111@gmail.com

Z. A. Duriagina · V. V. Kulyk · V. I. Vavrukh · P. Ya. Lyutyy · T. M. Kovbasiuk · I. A. Lemishka
Department of Materials Science and Engineering, Lviv Polytechnic National University, 12 S. Bandera Str., Lviv 79000, Ukraine
e-mail: zduriagina@ukr.net

V. V. Kulyk
e-mail: kulykvolodymyrvolodymyrovych@gmail.com

V. I. Vavrukh
e-mail: vavrukh.valentyna@gmail.com

P. Ya. Lyutyy
e-mail: pavlo_lyutyy@ukr.net

T. M. Kovbasiuk
e-mail: felcproject@gmail.com

I. A. Lemishka
e-mail: mzihor@ukr.net

Z. A. Duriagina
Department of Materials Engineering, The John Paul II Catholic University of Lublin, 14 Racławickie Al., 20-950 Lublin, Poland



O. Fesenko and L. Yatsenko (eds.), *Nanomaterials and Nanocomposites, Nanostructure Surfaces, and Their Applications*, Springer Proceedings in Physics 279,
https://doi.org/10.1007/978-3-031-18096-5_10

manufactured with electron arc melting. As-cast and thermomechanically deformed series were examined. Beam specimens were cut of blanks, grinded, and polished to reach a good surface quality. Strength tests of specimen series were performed under three-point bending in a temperature range of 20–1000 °C. Single-edge notch beam (SENB) tests under three-point bending of specimen series were carried out in a temperature range of 20–900 °C for estimating fracture toughness of materials. Based on the constructed dependences of fracture toughness and strength on testing temperature for the specimen series as well as the microstructure and failure micromechanism analyses, the role of ultrafine alloying elements in achieving good high-temperature strength and fracture toughness of the studied composites was substantiated.

## 1 Introduction

Nowadays, to ensure required operating life of parts and products in hard operating conditions, there is a need to use high-strength and oxidation-resistant materials like advanced ceramic materials (silicon carbide, silicon nitride, alumina, zirconia, etc.) and various composites. Owing to their high-temperature strength and chemical inertness, these materials can be operated under high pressure or vacuum, high temperature, radiation, corrosion, etc. [1–10].

In contrast to conventional titanium alloys, an operating temperature of which is limited by 300–500 °C, advanced Ti-based composites possess high fracture toughness and strength under bend and tensile loading in the temperature range of 20–650 °C. Owing to their high strength-to-weight ratio, these composites are promising for applications in components of modern engines (aircraft, rocket, and internal combustion ones) as well as other power equipment (compressors, gas turbines, fuel cells, etc.) [11–23]. However, there is a need to increase their operating temperature range up to 700–800 °C. Under such conditions, these materials must meet the requirements on high strength and crack growth resistance as well as corrosion resistance [11, 24–26]. This should be taken into account while developing new materials and improving microstructure and mechanical properties of already existing ceramics and composites [27–34]. The substantiation of chemical composition and processing and treatment modes are crucial issues in improving the phase

V. V. Vira
Department of Strength of Materials and Structural Mechanics, Lviv Polytechnic National University, 12 S. Bandera Str., Lviv 79000, Ukraine
e-mail: viravolodymyr@gmail.com

M. Ya. Holovchuk
Department of Corrosion and Corrosion Protection, Karpenko Physico-Mechanical Institute of the NAS of Ukraine, 5 Naukova Str., Lviv 79060, Ukraine
e-mail: golovchuk86@gmail.com

compositions, microstructure, and mechanical properties of the developed materials [35–44].

Depending on the chemical composition, Ti and Cr-based composites may comprise some amount of high-temperature phases, namely, silicides, aluminides, MAX phases, etc. [45–57]. In particular, MAX phases are formed as quite distinct regions along the boundaries of titanium or chromium grains in Ti and Cr based composites [53, 58, 59]. It was shown in a number of works that MAX phases are of great practical interest in terms of creating materials for use in mechanical engineering, aerospace and nuclear industries [2, 59, 60]. MAX phases are ternary layered compounds corresponding to the conditional formula $M_{n+1}AX_n$ ($n = 1, 2, 3$ …), where M is a transition metal of the *d*-group (Sc, Ti, V, Cr, Zr, Nb, Mo, Hf, Ta), A is an element of the *p*-group (Si, Ge, Al, Ga, S, P, Sn, As, Cd, I, Tl, Pb), and X is carbon or nitrogen [61].

Among a variety of MAX phases, $Ti_3SiC_2$ MAX phase is not an ideal self-healing material. Its self-healing performance can be improved somewhat by partially replacing Si with Al due to the faster diffusion and oxidation of Al and a good oxidation resistance of $Al_2O_3$. By partially replacing the A atoms of $Ti_3SiC_2$ with Al, $Ti_3Si_{1-x}Al_xC_2$ solid solutions are formed [18, 58, 62] that improves oxidation resistance of the material. Besides, in $Ti_2AlC$ MAX phase, the oxidation temperature of Al could be lowered to 900 °C by partially replacing Al with Sn [18, 55, 58, 63]. At temperatures below 600 °C, $SnO_2$ can be already formed in $Ti_2Al_{1-x}Sn_xC$. This may serve as an attractive crack filling potential for $Ti_2Al_{1-x}Sn_xC$ at lower temperatures. However, no significant increase in the mechanical strength was found in such a composite due to the poor mechanical strength of the $SnO_2$ and the poor bond strength [58, 63].

It is known that MAX phases belong to the hexagonal crystal system. Similarly to other materials belonging to the hexagonal crystal system [57, 58, 61, 62], there exists a possibility to fabricate textured bulk MAX phases. Pressure-assisted sintering, e.g., HP and SPS, are the most widely used techniques to prepare textured bulk MAX phases. As a result, the material consists of plate-like grains preferentially oriented under external conditions (e.g., a magnetic field or a uniaxial pressure). In contrast to the mentioned fabrication techniques, spark plasma sintering or direct hot pressing of MAX phases does not allow formation of highly textured microstructures, but may result in formation comparatively distinct MAX phase regions along the boundaries of titanium grains in Ti and Cr-based composites [13, 58, 59, 64–67].

It is also known that textured bulk MAX phases have anisotropic properties due to the lamellar crystal structure [58, 61]. This is a reason of high mechanical strength and crack growth resistance of these materials along specific directions and make them applicable to more harsh service environments.

Strength and wear resistance tests of ceramic and composite materials are widely used to estimate the bearing capacity of the corresponding products [68–70]. However, to prevent the degradation of microstructure of materials in environmentally assisted harsh conditions [71, 72], there is a need to obtain material resistive to microstructural changes in such conditions [6, 73–78]. Microhardness and fracture toughness serve as characteristics of material for estimating its resistance to the

nucleation and growth of microcracks. For this purpose, the indentation test as one of the simplest known mechanical method is used [68, 79, 80]. Based on the indentation technique, a variety of loading schemes and formulas for calculating fracture toughness of materials were proposed [70–72, 79, 81, 82]. Thus, to develop a new ceramic or composite material with required physical and mechanical properties, it should be studied in terms of strength and crack growth resistance and their relations to the chemical and phase compositions.

The work is aimed at evaluating the effect of ultrafine alloying elements on phase composition, high-temperature strength, fracture toughness, and fracture micromechanisms of Ti–Si–X and Ti–Cr–X composites.

## 2 Materials and Methods

In this work, titanium-based composites of various systems have been studied. The composites were prepared from raw materials by arc melting in an argon atmosphere on a water-cooled copper hearth [59, 64]. The purity of the elements was as follows: Ti > 99.6 at%; Cr > 99.99 at%; and Si, C, Al, Sn, Zr > 99.99 at%. After melting, ingots were annealed at 1400 °C for 5 min. In some cases (composites 2 and 3, Table 1), ingots were rolled at a temperature of 1050 °C with applying the thermo-mechanical deformation of about 40%.

Beam specimens 5.0 × 7.5 × 50 mm in size were machined from ingots or blanks, grinded, and polished (Table 1).

Strength tests of beam specimens were performed under three-point bending in a temperature range of 20–1000 °C. The fracture stresses ($\sigma_f$) were calculated using the "stress–flexure" diagrams at $P = P_{\max}$ by the equation [25, 32, 36, 76]

$$\sigma_f = \frac{1.5 \cdot P_{\max} \cdot L}{b \cdot t^2} \tag{1}$$

where $P_{\max}$ is the maximum load (N); $L$ is the span between two supporting rollers (mm); $b$ and $t$ are the specimen width and thickness (mm).

To characterize crack growth resistance of materials [83–86], along with microhardnes [87, 88], a fracture toughness characteristic, namely, the critical stress intensity factor (SIF) $K_{\text{Ic}}$ is often used. One of the simplest methods of estimation of the fracture toughness is an indentation method implementing a variety of formulas

**Table 1** Types of the investigated composited and their marking

| Composite marking | System |
|---|---|
| 1 | Ti–Si–Al–Sn–C |
| 2 | Ti–Si–Al–Zr–C |
| 3 | Ti–Si–Al–Zr–C |
| 4 | Ti–Cr–Al–C |

for calculating the SIF [89–98]. For a lot of materials, the $K_{Ic}$ values calculated by some of these formulas are consistent with those obtained by conventional methods of fracture mechanics [79, 98, 99]. Among the last ones, a single-edge notch beam (SENB) test [100–102] is widely used to estimate fracture toughness of ceramic and composite materials. This method was thoroughly described in [99].

In our work, fracture toughness tests of specimen series were performed under three-point bending in a temperature range of 20–900 °C using the mentioned SENB test method. For estimating the critical SIF of materials corresponding formulas [100–102] were used.

At least three specimens were used for each test temperature of corresponding test methods.

A scanning electron microscope (SEM) Carl Zeiss EVO-40XVP equipped with an INCA Energy 350 system was used for the study of microstructure and fracture surface morphology of specimens and an energy-dispersive X-ray (EDX) microanalysis of chemical composition of the materials both in secondary electron (SE) and back-scattered electron (BSE) imaging modes.

X-ray powder diffraction data was obtained by using a X-ray diffractometer (Aeris, Malvern Panalytical) with Cu Kα radiation operated at a voltage of 40 kV and a current of 15 mA. The angular range was 20°–90° and a step was 0.0217°. The X-ray diffraction (XRD) phase analysis was perfomed using Highscore software and referenced with the International Center for Diffraction Data (ICDD). All procedures including indexing, structure solutions, and refinement of profile and structural parameters were performed with the WinCSD [103] program package.

## 3 Results and Discussion

The microstructure and mechanical behavior of the titanium-based composites of Ti–Si–X and Ti–Cr–X systems in a wide temperature range have been studied.

### *3.1 XRD Analysis of the Studied Composites*

*Ti–Si–Al–Sn–C composite (1).* The XRD patterns of the composites under study (Fig. 1) show in detail the peculiarities of their phase balances. The XRD pattern of composite 1 (Ti–Si–Al–Sn–C system) contains only peaks of the α-Ti and $TiC_{0.67}$ phases (Fig. 1a). The α-Ti phase percentage was found to be about 90 wt%, whereas the $TiC_{0.67}$ phase percentage was about 10 wt%. The morphology of these phases was investigated in details using the microstructure images made at various magnifications. At a low magnification, one can see quite homogeneous microstructure of the Ti–Si–Al–Sn–C composite (Fig. 2a). At a higher magnification, we can observe distinct microstructural components of this composite (Fig. 2b). According to a

general EDX analysis (spectrum 1 in Fig. 2b and Table 2), this material contains 87.41 wt% Ti, 6.09 wt% Al, 3.15 wt% Si, and 3.35 wt% Sn. The results of EDX analysis showed some difference in chemical composition of the Ti–Si–Al–Sn–C composite material as compared to the results of XRD analysis. According to EDX analysis (Fig. 2b and Table 2), this material is a metal-matrix composite of Ti–Si–Al–Sn–C system with high titanium content. It possibly comprises the titanium matrix phase, $Ti_5Si_3$ phase, $Ti_3SiC_2$ MAX phase, and titanium carbide phase.

The titanium phase (α-Ti of about 87 wt% Ti, spectrum 2 in Fig. 2b and Table 2) with some amounts of aluminum (6.26 wt%), silicon (2.39 wt%), and tin (3.88 wt%) is a matrix phase. The total amount of the α-Ti phase estimated optically using the microstructure image (Fig. 2b) is about 66–70 vol%.

The $Ti_5Si_3$ phase with small amounts of aluminum (4.35 wt%) and tin (2.2 wt%) looks like thin elongated curved areas of light-gray color about 25 μm in length (spectrum 3 in Fig. 2b). These areas are located at the boundaries of titanium lamella

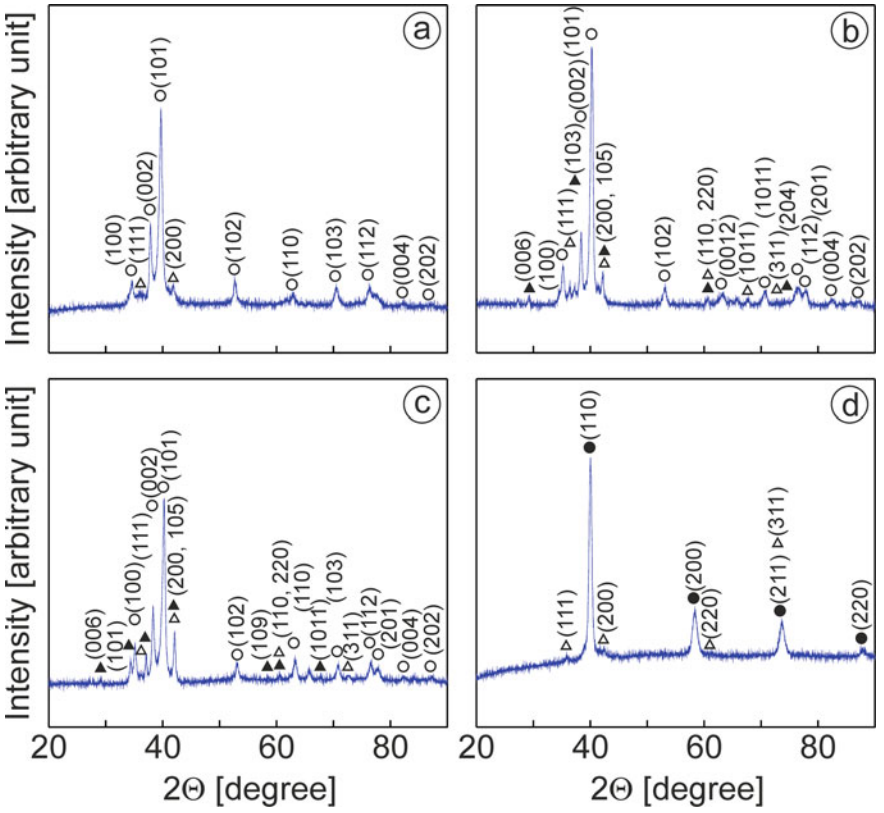


**Fig. 1** XRD patterns of the investigated composites **a** 1, **b** 2, **c** 3, and **d** 4 (Table 1) showing peaks for the α-Ti (light circles), Ti(Cr) (dark circles), $TiC_{0.67}$ (light triangles), and $Ti_3SiC_2$ phases (dark triangles) and corresponding Miller indices (in parentheses)

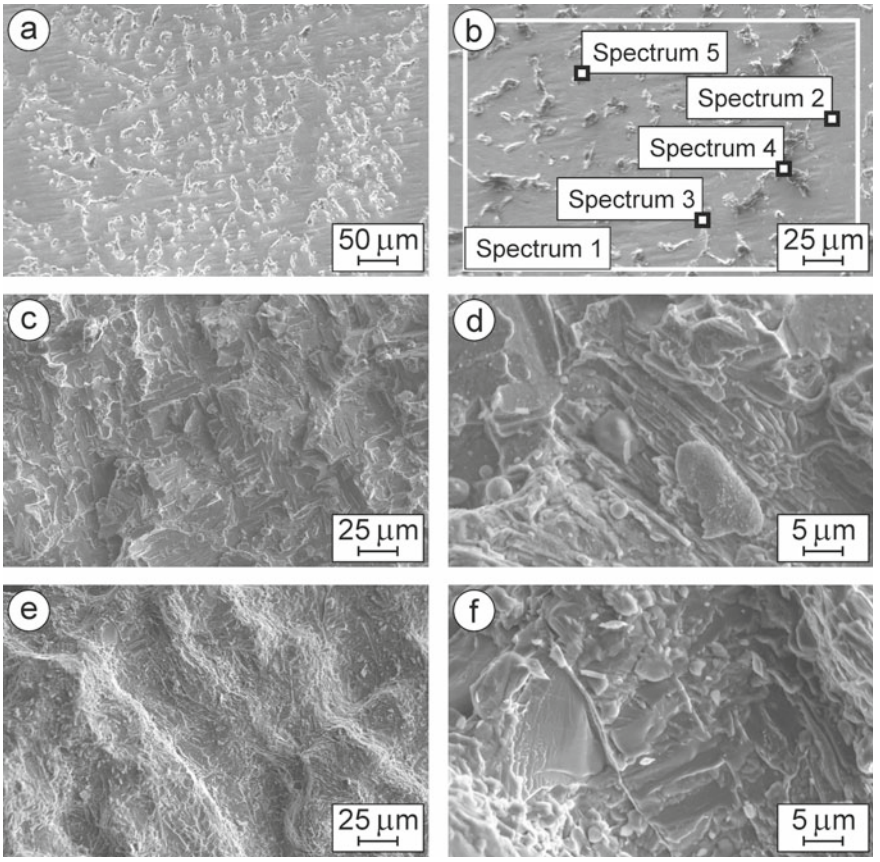


**Fig. 2** SEM **a, b** microstructures (SE images) with marked zones of **b** general (spectrum 1) and local (spectra 2, 3, 4, and 5) EDX analyses, and **c–f** fractography (SE images) of specimens of composite 1 after fracture toughness tests at **c, d** 20 °C and **e, f** 650 °C (Table 1)

**Table 2** The data of the EDX spectra 1–5 marked in Fig. 2 for a specimen of composite 1 (Table 1)

| Chemical element and X-ray series | Spectra | | | | | | | | | |
|---|---|---|---|---|---|---|---|---|---|---|
| | 1 | | 2 | | 3 | | 4 | | 5 | |
| | wt% | at% | wt% | at% | wt% | at% | wt% | at% | wt% | at% |
| C K | – | – | – | – | – | – | 14.88 | 38.85 | 24.62 | 54.32 |
| Al K | 6.09 | 10.31 | 6.26 | 10.66 | 4.35 | 6.98 | 3.25 | 3.77 | 2.74 | 2.69 |
| Si K | 3.15 | 5.12 | 2.39 | 3.92 | 12.44 | 19.14 | 9.87 | 11.04 | 9.68 | 9.13 |
| Ti K | 87.41 | 83.28 | 87.47 | 83.92 | 81.01 | 73.08 | 69.95 | 45.80 | 59.80 | 33.08 |
| Fe K | – | – | – | – | – | – | – | – | 0.21 | 0.10 |
| Cd L | – | – | – | – | – | – | – | – | 1.31 | 0.31 |
| Sn L | 3.35 | 1.29 | 3.88 | 1.50 | 2.20 | 0.80 | 2.05 | 0.54 | 1.64 | 0.37 |

packets. The total area occupied by them (Fig. 2b) is about 11–12 vol%. The $Ti_5Si_3$ phase was not detected by XRD analysis because of its small content.

The $Ti_3SiC_2$ MAX phase with small amounts of aluminum (3.25 wt%) and tin (2.05 wt%) looks like thick elongated areas of dark-gray color about 15 μm in size (spectrum 4 in Fig. 2b). These areas are located at the boundaries of titanium lamella packets similar to the $Ti_5Si_3$ phase. The total amount of the MAX phase (Fig. 2b) is about 14–15 vol%. Both the $Ti_5Si_3$ phase and the $Ti_3SiC_2$ MAX phase were not detected by XRD analysis because of their small content.

The titanium carbide phase ($TiC_{0.67}$, spectrum 5 in Fig. 2b) is in the form of distinct round-shaped particles of dark-gray color about 3 μm in size. The particles are distributed uniformly both in the matrix the α-Ti phase and at the boundaries of titanium lamella packets. The total area occupied by them (Fig. 2b) is about 5–7 vol%. Besides, small amounts of the $Ti_5Si_3$ phase and the $Ti_3SiC_2$ MAX phase are probably neighboring these carbide phase particles since some amount of silicon (9.68 wt%), along with small amounts of aluminum (2.74 wt%), iron (0.21 wt%), cadmium (1.31 wt%), and tin (1.64 wt%), were also detected in these areas.

*Ti–Si–Al–Zr–C composite (2).* The XRD pattern of composite 2 (Ti–Si–Al–Zr–C system) contains peaks of the α-Ti, $TiC_{0.67}$, and $Ti_3SiC_2$ MAX phases (Fig. 1b). Its phase composition was found to be as follows: α-Ti phase (about 70 wt%), $TiC_{0.67}$ phase (about 12 wt%), and $Ti_3SiC_2$ MAX phase (about 18 wt%). The microstructure image of the Ti–Si–Al–Zr–C composite made at a low magnification showed its homogeneous microstructure (Fig. 3a). The microstructure image of a higher magnification presents uniformly distributed areas of arbitrary shapes differing in colors (Fig. 3b). A general EDX analysis (spectrum 1 in Fig. 3b and Table 3) showed 76.79 wt% Ti, 6.77 wt% C, 3.88 wt% Al, 5.75 wt% Si, and 6.81 wt% Zr in this material. Thus, this material is a metal-matrix composite of Ti–Si–Al–Zr–C system possibly comprising the titanium matrix phase, $(Ti, Zr)_5Si_3$ phase, $Ti_3SiC_2$ MAX phase, and titanium carbide phase.

The α-Ti phase (89.65 wt% Ti, spectrum 2 in Fig. 3b and Table 3) with some amounts of aluminum (5.14 wt%), silicon (1.1 wt%), and zirconium (4.11 wt%) is a matrix phase. The total amount of the α-Ti phase (Fig. 3b) is about 52–55 vol%.

The $(Ti, Zr)_5Si_3$ phase looks like round-shaped particles of dark-gray color about 5 μm in size (spectrum 3 in Fig. 3b). These areas are adjacent to the titanium lamella packets. The total area occupied by them (Fig. 3b) is about 4–6 vol%. Besides, small amounts of the $Ti_3SiC_2$ MAX phase and the $TiC_{0.67}$ phase are probably neighboring these particles since some amount of carbon (6.97 wt%), along with a small amount of aluminum (1.46 wt%), was also detected in these areas. However, the $(Ti, Zr)_5Si_3$ phase was not revealed by XRD analysis because of its small percentage.

The titanium carbide phase $TiC_{0.67}$ with small amount of the $Ti_3SiC_2$ MAX phase and also small amounts of aluminum (5.09 wt%) and zirconium (2.69 wt%) looks like textured bulk MAX phase regions about 35–60 μm in size consisting of thin lamellae (spectrum 4 in Fig. 3b). These regions are uniformly distributed in the titanium matrix. The total amount of these regions (Fig. 3b) is about 35–45 vol%.

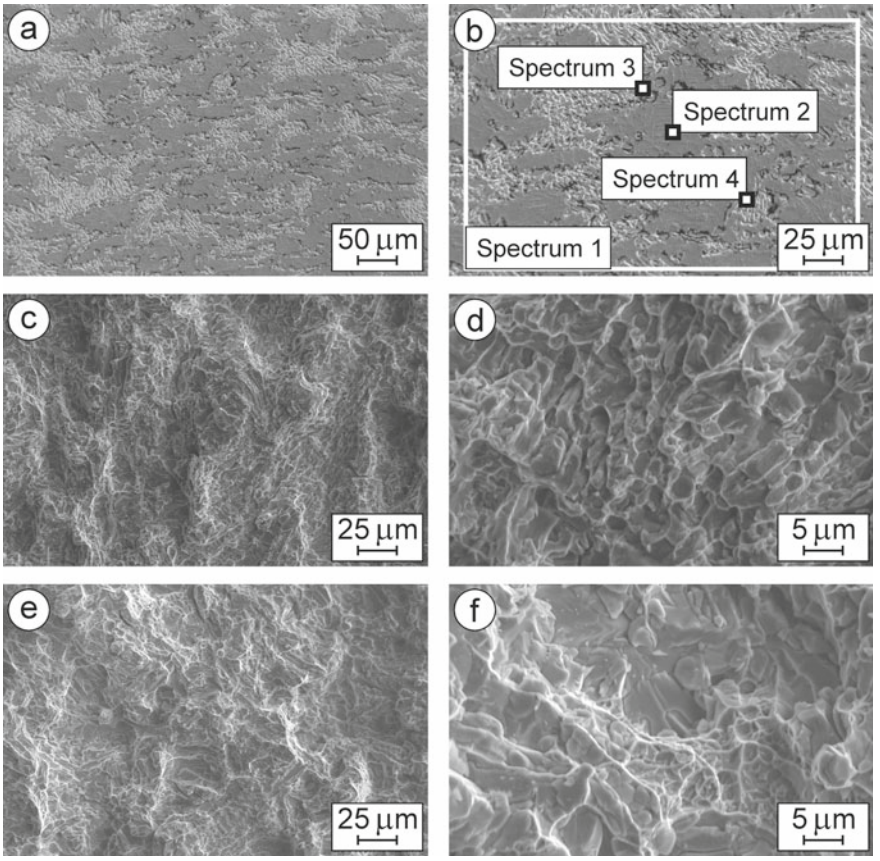


**Fig. 3** SEM **a, b** microstructures (SE images) with marked zones of **b** general (spectrum 1) and local (spectra 2, 3, and 4) EDX analyses, and **c–f** fractography (SE images) of specimens of composite 2 after fracture toughness tests at **c, d** 20 °C and **e, f** 700 °C (Table 1)

**Table 3** The data of the EDX spectra 1–4 marked in Fig. 3 for a specimen of composite 2 (Table 1)

| Chemical element and X-ray series | Spectra | | | | | | | |
|---|---|---|---|---|---|---|---|---|
| | 1 | | 2 | | 3 | | 4 | |
| | wt% | at% | wt% | at% | wt% | at% | wt% | at% |
| C K | 6.77 | 21.75 | – | – | 6.97 | 21.55 | 7.30 | 22.94 |
| Al K | 3.88 | 5.56 | 5.14 | 8.88 | 1.46 | 2.01 | 3.07 | 4.29 |
| Si K | 5.75 | 7.91 | 1.10 | 1.82 | 19.69 | 26.04 | 10.62 | 14.26 |
| Ti K | 76.79 | 61.90 | 89.65 | 87.20 | 57.46 | 44.53 | 69.10 | 54.41 |
| Zr L | 6.81 | 2.88 | 4.11 | 2.10 | 14.42 | 5.87 | 9.91 | 4.10 |

*Ti–Si–Al–Zr–C composite (3).* The XRD pattern of composite 3 (Ti–Si–Al–Zr–C system) is similar to that of composite 2 and contains peaks of the α-Ti, $TiC_{0.67}$, and $Ti_3SiC_2$ MAX phases (Fig. 1c). Its phase composition is as follows: α-Ti phase (about 75 wt%), $TiC_{0.67}$ phase (about 17 wt%), and $Ti_3SiC_2$ MAX phase (about 8 wt%). The microstructure image of the Ti–Si–Al–Zr–C composite made at a low magnification showed a quite homogeneous microstructure with some resemblance to the microstructure of composite 2 (Fig. 4a). The microstructure image of a higher magnification presents randomly distributed areas of arbitrary shapes (Fig. 4b). As a result of a general EDX analysis (spectrum 1 in Fig. 4b and Table 4), 83.1 wt% Ti, 5.07 wt% Al, 5.94 wt% Si, and 5.89 wt% Zr were found in this material. Unexpectedly, no signs of carbon were detected. Like composite 2, this material is a metal-matrix composite of Ti–Si–Al–Zr–C system possibly comprising the α-Ti matrix phase, $(Ti, Zr)_5Si_3$ phase, $Ti_3SiC_2$ MAX phase (only according to XRD analysis), and titanium carbide phase.

The α-Ti matrix phase (89 wt% Ti, spectrum 2 in Fig. 4b and Table 4) with some amounts of aluminum (5.99 wt%), silicon (1.07 wt%), and zirconium (3.94 wt%) is presented in an amount of about 56–60 vol%.

The $(Ti, Zr)_5Si_3$ phase with a small amount of aluminum (2.07 wt%) looks like particles of arbitrary shapes about 5–25 μm in size united in colonies or distributed randomly (spectrum 3 in Fig. 4b). They occupy the total area of about 26–30 vol% (Fig. 4b). For an unknown reason, this phase was not detected by XRD analysis.

The $TiC_{0.67}$ phase with a small amount of the $Ti_3SiC_2$ MAX phase and some amounts of aluminum (5.09 wt%) and zirconium (2.69 wt%) looks like particles of arbitrary shapes about 1–5 μm in size distributed randomly in titanium matrix (spectrum 4 in Fig. 4b). The total amount of these particles (Fig. 4b) is about 14–18 vol%.

*Ti–Cr–Al–C composite (4).* The XRD pattern of composite 4 (Ti–Cr–Al–C system) contains peaks of the Ti(Cr) and $TiC_{0.67}$ phases (Fig. 1b). Its phase composition was found to be as follows: Ti(Cr) phase (about 78 wt%) and $TiC_{0.67}$ phase (about 22 wt%). At a low magnification, distinctly grained microstructure of the Ti–Cr–Al–C composite can be observed (Fig. 5a). The microstructure image of a higher magnification presents grains of a matrix phase with uniformly distributed tiny particles inside and the fringe-like grain boundary regions. The fringes consist of needle-shaped particles differing in colors (Fig. 5b). A general EDX analysis (spectrum 1 in Fig. 5b and Table 5) showed 54.4 wt% Ti, 37.34 wt% Cr, 5.12 wt% C, and 3.14 wt% Al in this material. The material presenting a metal-matrix composite of Ti–Cr–Al–C system possibly comprises the Ti(Cr) matrix phase, $Al_2O_3$ phase, and titanium/chromium carbide phase.

The Ti(Cr) matrix phase comprises titanium (57.3 wt%, spectrum 2 in Fig. 5b and Table 5) and chromium (39.2 wt%) with some amount of aluminum (3.5 wt%). The total amount of the Ti(Cr) phase (Fig. 5b) is about 66–72 vol%.

The titanium/chromium carbide phase and the $Al_2O_3$ phase (spectrum 3 in Fig. 5b) containing in total 49.17 wt% Ti, 25.14 wt% Cr, 14.3 wt% C, 8.08 wt% O, and 3.31

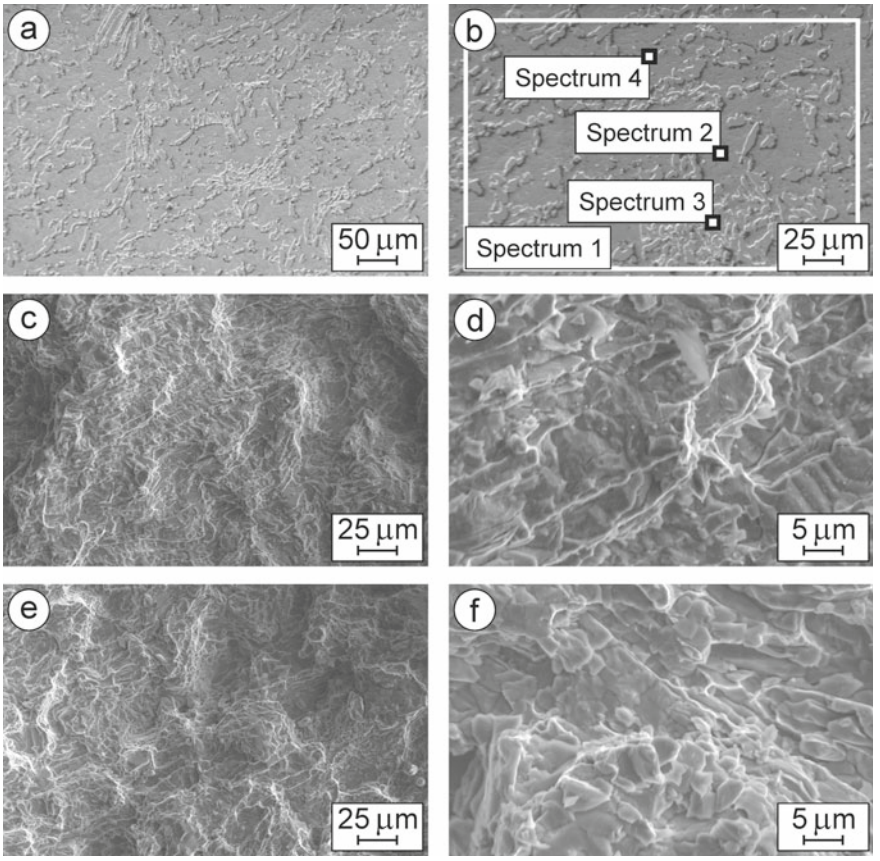


**Fig. 4** SEM **a, b** microstructures (SE images) with marked zones of **b** general (spectrum 1) and local (spectra 2, 3, and 4) EDX analyses, and **c–f** fractography (SE images) of specimens of composite 3 after fracture toughness tests at **c, d** 20 °C and **e, f** 700 °C (Table 1)

**Table 4** The data of the EDX spectra 1–4 marked in Fig. 4 for a specimen of composite 3 (Table 1)

| Chemical element and X-ray series | Spectra | | | | | | | |
|---|---|---|---|---|---|---|---|---|
| | 1 | | 2 | | 3 | | 4 | |
| | wt% | at% | wt% | at% | wt% | at% | wt% | at% |
| C K | – | – | – | – | – | – | 11.22 | 32.70 |
| Al K | 5.07 | 8.55 | 5.99 | 10.27 | 2.07 | 3.32 | 5.09 | 6.61 |
| Si K | 5.94 | 9.61 | 1.07 | 1.76 | 20.85 | 32.09 | 0.88 | 1.09 |
| Ti K | 83.10 | 78.90 | 89.00 | 85.97 | 65.45 | 59.08 | 80.12 | 58.57 |
| Zr L | 5.89 | 2.94 | 3.94 | 2.00 | 11.63 | 5.51 | 2.69 | 1.03 |

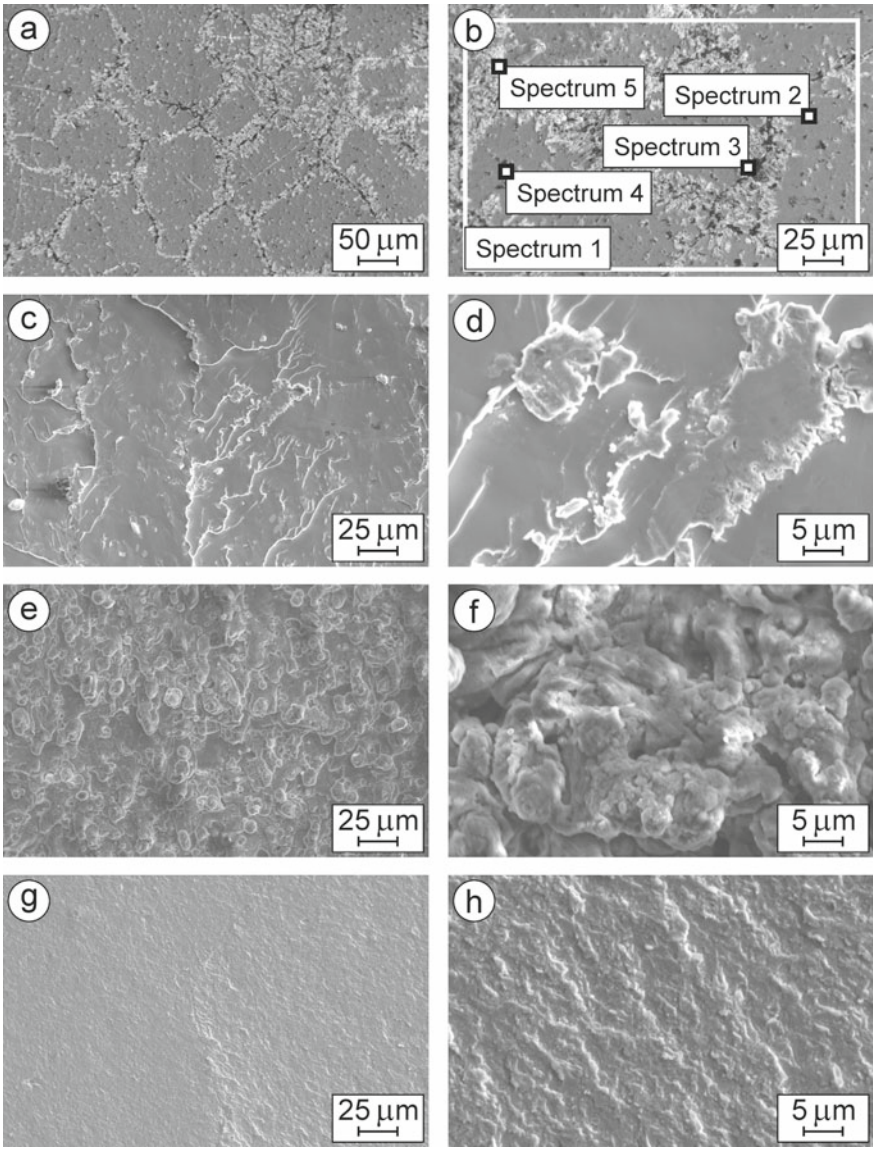


**Fig. 5** SEM **a, b** microstructures (SE images) with marked zones of **b** general (spectrum 1) and local (spectra 2, 3, 4, and 5) EDX analyses, and **c–h** fractography (SE images) of specimens of composite 4 after fracture toughness tests at **c, d** 20 °C, **e, f** 700 °C, and **g, h** 800 °C (Table 1)

**Table 5** The data of the EDX spectra 1–5 marked in Fig. 5 for a specimen of composite 4 (Table 1)

| Chemical element and X-ray series | Spectra | | | | | | | | | |
|---|---|---|---|---|---|---|---|---|---|---|
| | 1 | | 2 | | 3 | | 4 | | 5 | |
| | wt% | at% | wt% | at% | wt% | at% | wt% | at% | wt% | at% |
| C K | 5.12 | 17.78 | – | – | 14.30 | 35.77 | 11.99 | 35.30 | 6.29 | 19.95 |
| O K | – | – | – | – | 8.08 | 15.17 | – | – | 3.86 | 9.20 |
| Al K | 3.14 | 4.85 | 3.50 | 6.23 | 3.31 | 3.69 | 2.98 | 3.91 | 2.74 | 3.87 |
| Ti K | 54.40 | 47.40 | 57.30 | 57.52 | 49.17 | 30.84 | 50.98 | 37.63 | 50.29 | 40.00 |
| Cr K | 37.34 | 29.97 | 39.20 | 36.25 | 25.14 | 14.53 | 34.05 | 23.16 | 36.82 | 26.98 |

wt% Al were detected at the grain boundaries in the areas of black color. The total amount of these areas (Fig. 5b) was about 4–6 vol%.

A local EDX analysis of a round-shaped particle of dark-gray color about 1 μm in size (spectrum 4 in Fig. 5b and Table 5) showed 50.98 wt% Ti, 34.05 wt% Cr, 11.99 wt% C, and 2.98 wt% Al. This particle probably was the titanium carbide phase $TiC_{0.67}$ identified by XRD analysis, whereas some amounts of chromium and aluminum were detected by EDX analysis in the surrounding Ti(Cr) matrix phase. The total amount of these carbide particles was about 10–12 vol%.

The thin needle-shaped particles of light-gray color about 15 μm in length (spectrum 5 in Fig. 5b) forming the fringe-like grain boundary regions and containg 50.29 wt% Ti, 36.82 wt% Cr, 6.29 wt% C, 3.86 wt% O, and 2.74 wt% Al present a mixture of the $TiC_{0.67}$ and $Al_2O_3$ phases that surrounds the Ti(Cr) phase grains. Their total amount is about 14–16 vol%. However, the $Al_2O_3$ phase was not detected by XRD analysis because of its small percentage.

In general, the subsequence of phases formation in the studied composites may be as follows: in the beginning of the solidification process, titanium carbides and titanium/zirconium silicides and MAX-phase were formed; then, the recrystallization of titanium/chromium grains occurred.

## *3.2 Mechanical Behavior of the Studied Composites and Microstructure Related Fracture Mechanisms*

The studied composites exhibited distinct temperature dependences of both strength and fracture toughness (Fig. 6). In particular, the composites 1 (Ti–Si–Al–Sn–C system), 2 (Ti–Si–Al–Zr–C system), and 3 (Ti–Si–Al–Zr–C system) showed high and invariant values of fracture toughness (Fig. 6b) in a temperature range of 20–500 °C. In this range, fracture toughness of these composites is about 20 $MPa{\cdot}m^{1/2}$. In contrast, the monotonously changing temperature dependences of strength (increasing for composite 1 and decreasing for composites 2 and 3, Fig. 6a) were revealed.

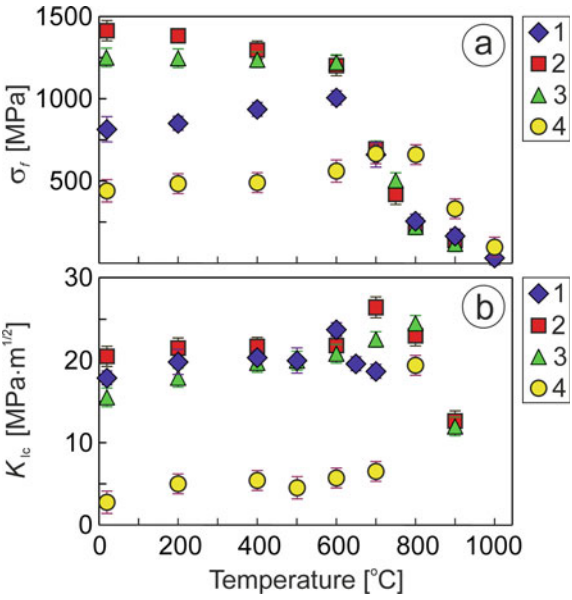


**Fig. 6** Temperature dependences of **a** strength and **b** fracture toughness of the studied composites (Table 1)

A specimen of composite 1 undergone to the fracture toughness test at 20 °C exhibited a distinct fracture surface (Fig. 2c, d) corresponding to a mixed fracture along the boundaries of titanium lamella packets and transgranular fracture across titanium grains in the case when a cleavage plane coincides with the direction of crack propagation. This fracture micromechanism is related to the comparatively high fracture toughness (Fig. 6b). Strength of this composite increased from about 760 MPa at 20 °C to 1000 MPa at 500 °C.

Fracture surface of a specimen of composite 2 tested at 20 °C (Fig. 3c, d) corresponds to a fracture along the boundaries of titanium lamella packets. No transgranular fracture across titanium grains occurred. Therefore, a coarse relief of fracture surface was formed that was a reason of high fracture toughness of the composite (Fig. 6b).

Similarly to this material, fracture surface of a specimen of composite 3 tested at 20 °C (Fig. 4c, d) exhibited a coarse relief corresponding to high fracture toughness of the composite (Fig. 6b).

Strength of composites 2 and 3 decreased from 1400 and 1250 MPa at 20 °C to 1230 MPa and 1240 MPa at 500 °C, respectively. Nevertheless, such a level of strength is high enough and meets the requirements to materials of this system.

A testing temperature in a range of 600–850 °C is critical for these three composites since for each composite a maximum of fracture toughness appeared on the corresponding dependence is shifted toward a certain temperature. Its location is related to the microstructural peculiarities of a composite, its chemical and phase compositions, as well as dominant fracture micromechanism.

For composite 1, a temperature above 600 °C is critical since it corresponds to the maximum of fracture toughness (Fig. 6b). A specimen undergone to the fracture toughness test at 650 °C exhibited blunted edges of titanium lamella packets (Fig. 2e), microregions of transverse fracture of thin $Ti_3SiC_2$ MAX phase lamellae (Fig. 2f), and signs of quazi brittle failure of the $Ti_5Si_3$ phase grains on fracture surface (Fig. 2f). The fracture toughness is as high as in the case of testing at 20 °C (Fig. 6b). Obviously, a transition from quazi brittle (at 600 °C) to high-temperature ductile fracture (at 650 °C) occurred that was followed by some lowering of fracture toughness (from 24 MPa·$m^{1/2}$ at 600 °C to 19 MPa·$m^{1/2}$ at 650 °C, Fig. 6b). Probably, tin also contributes to the transition process. Strength of this composite decreased from about 1000 MPa at 600 °C to 650 MPa at 700 °C (Fig. 6a).

A temperature corresponding to the maximum of fracture toughness for composite 2 is about 700 °C (Fig. 6b). Such a shift by 100 °C compared to composite 1 is important in terms of high-temperature mechanical stability of the studied composites. Fracture surface of a specimen of composite 2 tested at 700 °C (Fig. 3e, f) exhibited a coarse relief with signs of plastic elongation of titanium grains corresponding to the highest fracture toughness of the composite among the tested ones (Fig. 6b). No transgranular fracture across titanium grains occurred and no signs of debonding between $Ti_5Si_3$ phase grains or $Ti_3SiC_2$ MAX phase lamellae and titanium matrix were detected (Fig. 3f).

For composite 3, in contrast to composite 2, a temperature corresponding to the maximum of fracture toughness is about 800 °C (Fig. 6b). However, the shift by 200 °C compared to composite 1 is rather related to a difference in phase compositions of these materials. On fracture surface of a specimen of composite 3 tested at 700 °C (Fig. 4e, f), a coarse relief of fracture along titanium lamella packets with an average size smaller than in composite 2, with signs of plastic elongation of titanium grains, was observed. Such fracture surface morphology is consistent with slightly lower fracture toughness of composite 3 than composite 2 (Fig. 6b). Similarly to composite 2, no transgranular fracture across titanium grains was found and no signs of debonding between the $(Ti, Zr)_5Si_3$ or $TiC_{0.67}$ or $Ti_3SiC_2$ MAX phase components and the α-Ti matrix phase were detected (Fig. 4f).

In contrast to mechanical behavior of above-mentioned materials, composite 4 showed invariant values of both strength (Fig. 6a) and fracture toughness (Fig. 6b) in a temperature range of 20–600 °C. Strength of this composite is about 500 MPa in this temperature range with a trend to increasing, whereas fracture toughness is about 5 MPa·$m^{1/2}$. Increased strength (up to 650 MPa at 700 and 800 °C, Fig. 6a) and fracture toughness of the composite (steep increase up to 19 MPa·$m^{1/2}$ at 800 °C, Fig. 6b) are the evidences of a change in the fracture micromechanism. Fracture surface of a specimen of composite 4 undergone to the fracture toughness test at 20 °C showed signs of transgranular cleavage fracture with separation of fringe-like grain boundary regions and the titanium carbide phase $TiC_{0.67}$ particles in places where the advancing crack crossed them (Fig. 5c, d). A different pattern of fracture surface was observed in a specimen of composite 4 after the fracture toughness test at 700 °C (Fig. 5e, f). Because of intense plasticization of the Ti(Cr) matrix phase at this temperature, multiple microregions of ductile metal surrounding each of titanium

carbide particles that are embodied into a Ti(Cr) matrix grains (Fig. 5e) with visible shear bands (Fig. 5f) as signs of plastic deformation of the matrix phase during crack growth can be seen. Such fracture micromechanism is related to temperature-assisted relaxation of stress in the crack tip vicinity that corresponds to some increase in fracture toughness of the material at 700 °C (Fig. 6b). Finally, a phenomenon of substantial increase in both strength (Fig. 6a) and fracture toughness of the composite (Fig. 6b) at 800 °C may be explained in terms of phase transformations due to high-temperature diffusion of some elements, in particular, aluminum and silicon [18, 58, 62]. This, in turn, causes a change in the fracture micromechanism [59, 76]. In this composite, high-temperature fracture occurred at 800 °C (Fig. 5g, h) with a steep increase in fracture toughness, due to diffusion of some elements and pore coalescence at the boundaries of the Ti(Cr) phase grains (Fig. 5h). No $TiC_{0.67}$ particles serve as stress concentrators, even in the places where the advancing crack crossed them (Fig. 5g). Thus, this temperature promotes quazi ductile character of crack growth resulted in striations (Fig. 5h) similar to fatigue crack growth in high-strength ductile materials at ambient temperature [59].

Thus, based on results of the strength test and fracture toughness tests along with analysis of microstructure peculiarities and fracture micromechanisms revealed in the whole temperature range investigated, the general tendencies in temperature dependent mechanical behavior of titanium-based composites have been substantiated. The Ti–Si–X composites can serve as high-temperature structural materials at an operating temperature up to 750 °C, whereas the Ti–Cr–X composite exhibits high-temperature stability at a higher temperature by about 50 °C.

## 4 Conclusions

In this work, mechanical behavior of the Ti–Si–X and Ti–Cr–X composites have been studied in a temperature range of 20–900 °C.

1. The microstructure peculiarities and phase composition of the studied composites were substantiated.
2. It was shown that strength and fracture toughness parameters are suitable for the characterization of mechanical behavior of the composites in the investigated temperature range.
3. The phenomenon of increased strength and fracture toughness of Ti–Cr–Al–C composite was revealed and explained in terms of the morphology of microstructural components and dominant fracture micromechanisms.

**Acknowledgements** The authors are deeply grateful to the staff of the Scientific Equipment Collective Use Center "Laboratory of Advanced Technologies, Creation and Physicochemical Analysis of a New Substances and Functional Materials" at Lviv Polytechnic National University (https://lpnu.ua/ckkno) for their kind help in performing X-ray diffraction studies.

## References


1. Li D, Dong Y, Zhang Z et al (2021) An as-cast Ti-V-Cr-Al light-weight medium entropy alloy with outstanding tensile properties. J Alloy Compd 877:160199. https://doi.org/10.1016/j.jallcom.2021.160199
2. Prikhna TA, Ostash OP, Kuprin AS et al (2021) A new MAX phases-based electroconductive coating for high-temperature oxidizing environment. Compos Struct 277:114649. https://doi.org/10.1016/j.compstruct.2021.114649
3. Liu Z, Yang J, Qian Y et al (2020) In-situ reaction synthesis and mechanical properties of quaternary MAX phase $(Cr_{2/3}Ti_{1/3})_3AlC_2$. Ceram Int 46(14):22854–22860. https://doi.org/10.1016/j.ceramint.2020.06.055
4. Shabri HA, Othman MHD, Mohamed MA et al (2021) Recent progress in metal-ceramic anode of solid oxide fuel cell for direct hydrocarbon fuel utilization: a review. Fuel Process Technol 212:106626. https://doi.org/10.1016/j.fuproc.2020.106626
5. Serbenyuk TB, Prikhna TO, Sverdun VB et al (2018) Effect of the additive of $Y_2O_3$ on the structure formation and properties of composite materials based on AlN–SiC. J Superhard Mater 40(1):8–15. https://doi.org/10.3103/S1063457618010021
6. Dobrzański LA, Dobrzański LB, Dobrzańska-Danikiewicz AD (2020) Additive and hybrid technologies for products manufacturing using powders of metals, their alloys and ceramics. Arch Mater Sci Eng 102(2):59–85. https://doi.org/10.5604/01.3001.0014.1525
7. Posuvailo VM, Kulyk VV, Duriagina ZA et al (2020) The effect of electrolyte composition on the plasma electrolyte oxidation and phase composition of oxide ceramic coatings formed on 2024 aluminium alloy. Arch Mater Sci Eng 105(2):49–55. https://doi.org/10.5604/01.3001.0014.5761
8. Cherepova TS, Dmytrieva HP, Dukhota OI et al (2016) Properties of nickel powder alloys hardened with titanium carbide. Mater Sci 52(2):173–179. https://doi.org/10.1007/s11003-016-9940-2
9. Bocanegra-Bernal MH, Díaz de la Torre S (2002) Phase transitions in zirconium dioxide and related materials for high performance engineering ceramics. J Mater Sci 37:4947–4971. https://doi.org/10.1023/A:1021099308957
10. Ropyak LY, Makoviichuk MV, Shatskyi IP et al (2020) Stressed state of laminated interference-absorption filter under local loading. Funct Mater 27(3):638–642. https://doi.org/10.15407/fm27.03.638
11. Budzianowski WM, Milewski J (2011) Solid-oxide fuel cells in power generation applications: a review. Recent Patents Eng 5(3):1650–2189. https://doi.org/10.2174/187221211797636926
12. Komatsu Y, Sciazko A, Shikazono N (2021) Isostatic pressing of screen printed nickel-gadolinium doped ceria anodes on electrolyte-supported solid oxide fuel cells. J Power Sources 485:229317. https://doi.org/10.1016/j.jpowsour.2020.229317
13. Kashkarov EB, Pushilina NS, Syrtanov MS et al (2021) Preceramic paper-derived $SiC_f/Ti_3Al(Si)C_2$ and $SiC_f/Ti_3SiC_2$ MAX-phase based laminates fabricated using spark plasma sintering. Scripta Mater 194:113696. https://doi.org/10.1016/j.scriptamat.2020.113696
14. Tabares E, Cifuentes SC, Jiménez-Morales A et al (2021) Injection moulding of porous MAX phase $Ti_3SiC_2$ without using space-holder. Powder Technol 380:96–105. https://doi.org/10.1016/j.powtec.2020.11.022
15. Perevislov SN, Sokolova TV, Stolyarova VL (2021) The $Ti_3SiC_2$ max phases as promising materials for high temperature applications: formation under various synthesis conditions. Mater Chem Phys 267:124625. https://doi.org/10.1016/j.matchemphys.2021.124625
16. Silvestroni L, Melandri C, Gonzalez-Julian J (2021) Exploring processing, reactivity and performance of novel MAX phase/ultra-high temperature ceramic composites: the case study of $Ti_3SiC_2$. J Eur Ceram Soc 41(12):6064–6069. https://doi.org/10.1016/j.jeurceramsoc.2021.05.029

17. Tan Y, Xia Y, Teng Z et al (2021) Synthesis and enhanced mechanical properties of compositionally complex MAX phases. J Eur Ceram Soc 41(8):4658–4665. https://doi.org/10.1016/j.jeurceramsoc.2021.03.027
18. Yu W, Pi X, Chen W et al (2021) Effects of A-site atoms in $Ti_2AlC$ and $Ti_3SiC_2$ MAX phases reinforced Mg composites: interfacial structure and mechanical properties. Mater Sci Eng A 826:141961. https://doi.org/10.1016/j.msea.2021.141961
19. Yu D, Tan Y (2021) Oxidation behaviors of compositionally complex MAX phases in air. Ceram Int 47(21):30188–30193. https://doi.org/10.1016/j.ceramint.2021.07.198
20. Du P, Zhu B, Yang X et al (2021) Toxic elements-free low-cost Ti-Fe-Si metallic glass biomaterial developed by mechanical alloying. J Alloy Compd 886:161290. https://doi.org/10.1016/j.jallcom.2021.161290
21. Wejrzanowski T, Haj Ibrahim S, Cwieka K et al (2018) Multi-modal porous microstructure for high temperature fuel cell application. J Power Sources 373:85–94. https://doi.org/10.1016/j.jpowsour.2017.11.009
22. Podhurska V, Vasyliv B (2012) Influence of NiO reduction on microstructure and properties of porous Ni–$ZrO_2$ substrates. In: Proceedings of the 3rd international conference on oxide materials for electronic engineering (OMEE-2012), Lviv, Ukraine, pp 293–294. https://doi.org/10.1109/OMEE.2012.6464761
23. Danilenko I, Lasko G, Brykhanova I et al (2017) The peculiarities of structure formation and properties of zirconia-based nanocomposites with addition of $Al_2O_3$ and NiO. Nanoscale Res Lett 12:125. https://doi.org/10.1186/s11671-017-1901-7
24. Dobrzański LA, Dobrzański LB, Dobrzańska-Danikiewicz AD (2020) Manufacturing technologies thick-layer coatings on various substrates and manufacturing gradient materials using powders of metals, their alloys and ceramics. J Achieve. Mater Manuf Eng 99(1):14–41. https://doi.org/10.5604/01.3001.0014.1598
25. Vasyliv BD, Podhurska VY, Ostash OP et al (2018) Effect of a hydrogen sulfide-containing atmosphere on the physical and mechanical properties of solid oxide fuel cell materials. Nanochemistry, biotechnology, nanomaterials, and their applications. Springer Proc Phys 214:475–485. https://doi.org/10.1007/978-3-319-92567-7_30
26. Kulyk VV, Vasyliv BD, Duriagina ZA et al (2021) The effect of water vapor containing hydrogenous atmospheres on the microstructure and tendency to brittle fracture of anode materials of YSZ–NiO(Ni) system. Arch Mater Sci Eng 108(2):49–67. https://doi.org/10.5604/01.3001.0015.0254
27. Milewski J, Lewandowski J, Miller A (2008) Reducing $CO_2$ emissions from a coal fired power plant by using a molten carbonate fuel cell. Proc ASME Turbo Expo 2:389–395. https://doi.org/10.1115/GT2008-50100
28. Milewski J, Lewandowski J (2009) Solid oxide fuel cell fuelled by biogases. Arch Thermodyn 30(4):3–12. https://www.imp.gda.pl/fileadmin/doc/imp_publishing/wimp/archives%20of%20thermodynamics/C_09_4.pdf
29. Dobrzański LA, Dobrzański LB, Dobrzańska-Danikiewicz AD (2020) Overview of conventional technologies using the powders of metals, their alloys and ceramics in Industry 4.0 stage. J Achieve Mater Manuf Eng 98(2):56–85. https://doi.org/10.5604/01.3001.0014.1481
30. Savka SS, Popovych DI, Serednytski AS (2017) Molecular dynamics simulations of the formation processes of zinc oxide nanoclusters in oxygen environment. Nanophysics, nanomaterials, interface studies, and applications. Springer Proc Phys 195:145–156. https://doi.org/10.1007/978-3-319-56422-7_11
31. Milewski J, Kupecki J, Szczęśniak A et al (2021) Hydrogen production in solid oxide electrolyzers coupled with nuclear reactors. Int J Hydrog Energy 46(72):35765–35776. https://doi.org/10.1016/j.ijhydene.2020.11.217
32. Vasyliv B, Podhurska V, Ostash O (2017) Preconditioning of the YSZ–NiO fuel cell anode in hydrogenous atmospheres containing water vapor. Nanoscale Res Lett 12:265. https://doi.org/10.1186/s11671-017-2038-4
33. Witz G, Shklover V, Steurer W et al (2007) Phase evolution in yttria-stabilized zirconia thermal barrier coatings studied by Rietveld refinement of X-ray powder diffraction patterns. J Am Ceram Soc 90(9):2935–2940. https://doi.org/10.1111/j.1551-2916.2007.01785.x

34. Clarke DR, Levi CG (2003) Material design for the next generation thermal barrier coatings. Annu Rev Mater Res 33:383–417. https://doi.org/10.1146/annurev.matsci.33.011403.113718
35. Smyrnova-Zamkova MY, Ruban OK, Bykov OI et al (2018) Physico-chemical properties of fine-grained powder in $Al_2O_3$–$ZrO_2$–$Y_2O_3$–$CeO_2$ system produced by combined method. Comp Theory Practice 18(4):234–240. https://kompozyty.ptmk.net/pliczki/pliki/1290_2018t04_maria-y-smyrnova-zamkova-.pdf
36. Vasyliv B, Milewski J, Podhurska V et al (2022) Study of the degradation of a fine-grained YSZ–NiO anode material during reduction in hydrogen and reoxidation in air. Appl Nanosci 12:965–975. https://doi.org/10.1007/s13204-021-01768-w
37. Smyrnova-Zamkova MY, Red'ko VP, Ruban OK et al (2017) The properties of nanocrystalline powder of 90% $Al_2O_3$–10% $ZrO_2$ (wt%) obtained via the hydrothermal synthesis/mechanical mixing. Nanosistemi Nanomater Nanotechnol 15(2):309–317. https://doi.org/10.15407/nnn.15.02.0309
38. Sukhova OV (2009) Influence of mechanisms of structure formation of interfaces in composites on their properties. Metallofiz Noveishie Tekhnol 31(7):1001–1012
39. Dudnik OV, Marek IO, Ruban OK et al (2020) Effect of heat treatment on the structure and phase composition of the nanosized powder based on a $ZrO_2$ solid solution. Powder Metall Met Ceram 59(1–2):1–8. https://doi.org/10.1007/s11106-020-00132-x
40. Efremenko VG, Chabak YG, Shimizu K et al (2017) Structure refinement of high-Cr cast iron by plasma surface melting and post-heat treatment. Mater Des 126:278–290. https://doi.org/10.1016/j.matdes.2017.04.022
41. Zhou XW, Shen YF, Jin HM (2011) Effect of deposition mechanism and microstructure of nano-ceria oxide addition on Ni-P coating by pulse electrodeposition. Adv Mater Res 326:151–156. https://doi.org/10.4028/www.scientific.net/AMR.326.151
42. Shevchenko AV, Lashneva VV, Ruban AK et al (2016) Synthesis and study of high-purity nanocrystalline powder of a solid solution of $CeO_2$ and $Y_2O_3$ in zirconium dioxide. Powder Metall Met Ceram 54(9–10):548–553. https://doi.org/10.1007/s11106-016-9748-5
43. Kujawa M, Suwak R, Dobrzański LA et al (2021) Thermal characterization of halloysite materials for porous ceramic preforms. Arch Mater Sci Eng 107(1):5–15. https://doi.org/10.5604/01.3001.0014.8189
44. Marek IO, Ruban OK, Redko VP et al (2019) Physicochemical properties of hydrothermal nanocrystalline $ZrO_2$–$Y_2O_3$–$CeO_2$ powders. Powder Metall Met Ceram 58(3–4):125–132. https://doi.org/10.1007/s11106-019-00055-2
45. Crossman FW, Yue AS (1971) Unidirectionally solidified Ti-TiB and Ti-$Ti_5Si_3$ eutectic composites. Met Trans 2:1545–1555
46. Zhao H, Hu L, Li C et al (2021) Influence of metallic Cr addition on the phase structure and mechanical properties of plasma-sprayed Ti-Si-C coatings. Ceram Int 47(12):17570–17579. https://doi.org/10.1016/j.ceramint.2021.03.075
47. Cao Z, Zhou P, Xiao X et al (2021) Investigation on Ti-Zr-Cr-Fe-V based alloys for metal hydride hydrogen compressor at moderate working temperatures. Int J Hydrog Energy 46(41):21580–21589. https://doi.org/10.1016/j.ijhydene.2021.03.247
48. Chiu WT, Wakabayashi K, Umise A et al (2021) Enhancement of mechanical properties and shape memory effect of Ti-Cr-based alloys via Au and Cu modifications. J Mech Behavior Biomed Mater 123:104707. https://doi.org/10.1016/j.jmbbm.2021.104707
49. Liu J, Xu J, Sleiman S et al (2021) Microstructure and hydrogen storage properties of Ti-V-Cr based BCC-type high entropy alloys. Int J Hydrog Energy 46(56):28709–28718. https://doi.org/10.1016/j.ijhydene.2021.06.137
50. Zhou J, Xu Y, Zhang Z et al (2020) Interdiffusion and atomic mobility in the bcc Ti-rich Ti-Cr-Mn system. Calphad 68:101747. https://doi.org/10.1016/j.calphad.2020.101747
51. Hong SH, Park SW, Park CH et al (2021) Relationship between phase stability and mechanical properties on near/metastable b-type Ti-Cr-(Mn) cast alloys J Alloy Compd 821:153516. https://doi.org/10.1016/j.jallcom.2019.153516
52. Kehal A, Saoula N, Abaidia SEH et al (2021) Effect of Ar/$N_2$ flow ratio on the microstructure and mechanical properties of Ti-Cr-N coatings deposited by DC magnetron sputtering on

AISI D2 tool steels. Surf Coat Technol 421:127444. https://doi.org/10.1016/j.surfcoat.2021.127444
53. Ivasyshyn A, Ostash O, Prikhna T et al (2016) Oxidation resistance of materials based on $Ti_3AlC_2$ nanolaminate at 600 °C in air. Nanoscale Res Lett 11:358. https://doi.org/10.1186/s11671-016-1571-x
54. Chiu WT, Ishigaki T, Nohira N et al (2021) Effect of Cr additions on the phase constituent, mechanical properties, and shape memory effect of near-eutectoid Ti-4Au towards the biomaterial applications. J Alloy Compd 867:159037. https://doi.org/10.1016/j.jallcom.2021.159037
55. Chiu WT, Wakabayashi K, Umise A et al (2021) Enhancement of the shape memory effect by the introductions of Cr and Sn into the β-Ti alloy towards the biomedical applications. J Alloy Compd 875:160088. https://doi.org/10.1016/j.jallcom.2021.160088
56. Zhao X, Sokol M, Barsoum MW et al (2021) Effect of grain orientation on the compressive response of highly oriented MAX phase $Ti_3SiC_2$. Mater Sci Eng A 809:140869. https://doi.org/10.1016/j.msea.2021.140869
57. Prikhna T, Ostash O, Basyuk T et al (2015) Thermal stability and mechanical characteristics of densified $Ti_3AlC_2$-based material. Solid State Phenom 230:140–143. https://doi.org/10.4028/www.scientific.net/SSP.230.140
58. Zhang Z, Duan X, Jia D et al (2021) On the formation mechanisms and properties of MAX phases: a review. J Eur Ceram Soc 41(7):3851–3878. https://doi.org/10.1016/j.jeurceramsoc.2021.02.002
59. Ostash OP, Ivasyshyn AD, Vasyliv BD et al (2006) High-temperature and cyclic corrosion crack resistance of alloys of the Ti–Si–Al–Zr system. Mater Sci 42(3):330–343. https://doi.org/10.1007/s11003-006-0087-4
60. Frommeyer G, Rosenkranz R, Ludecke C (1990) Microstructure and properties of the refractory intermetallic $Ti_5Si_3$ compound and the unidirectionally solidified eutectic Ti-$Ti_5Si_3$ alloy. Metallkunde 81:307–313
61. Barsoum M (2000) The $M_{n+1}AX_n$ phases: a new class of solids. Prog Solid State Chem 28(2000):201–281. https://doi.org/10.1016/S0079-6786(00)00006-6
62. Liu R, Tane M, Kimizuka H et al (2021) Elastic isotropy originating from heterogeneous interlayer elastic deformation in a $Ti_3SiC_2$ MAX phase with a nanolayered crystal structure. J Eur Ceram Soc 41(4):2278–2289. https://doi.org/10.1016/j.jeurceramsoc.2020.11.026
63. Park MS, Chiu WT, Nohira N et al (2021) Effects of Cr and Sn additives on the martensitic transformation and deformation behavior of Ti-Cr-Sn biomedical shape memory alloys. Mater Sci Eng A 822:141668. https://doi.org/10.1016/j.msea.2021.141668
64. Mazur VI, Taran YN, Kapustnikova SV et al (1994) Titanium matrix composites. US Patent, No. 5366570, 22.11.1994
65. Vasyliv B, Ivasyshyn A, Ostash O et al (2004) High-temperature fatigue crack growth resistance of thermo-mechanically and heat treated cast Ti–Si–Al–Zr composites. Metallic materials with high structural efficiency. Kluwer Academic Publishers, The Netherlands, pp 235–240
66. Vasyliv BD, Ivasyshyn AD, Ostash OP et al (2002) Kinetics of corrosion-fatigue cracks in Ti–Si cermet composite. Mater Sci 38(2):220–224. https://doi.org/10.1023/A:1020990103898
67. Ostash OP, Ivasyshyn AD, Vasyliv BD et al (2002) Influence of the structure and asymmetry of loading cycles on the cyclic crack resistance of Ti–Si composites. Mater Sci 38(1):55–61. https://doi.org/10.1023/A:1020120714703
68. Jeong K-W, Han J-S, Yang G-U et al (2021) Influence of preaging temperature on the indentation strength of 3Y–TZP aged in ambient atmosphere. Materials 14:2767. https://doi.org/10.3390/ma14112767
69. Gaddam A, Brazete DS, Neto AS et al (2021) Three-dimensional printing of zirconia scaffolds for load bearing applications: study of the optimal fabrication conditions. J Am Ceram Soc 104(9):4368–4380. https://doi.org/10.1111/jace.17874

70. Ji SH, Kim DS, Park MS et al (2021) Sintering process optimization for 3YSZ ceramic 3D-printed objects manufactured by stereolithography. Nanomaterials 11:192. https://doi.org/10.3390/nano11010192
71. Tao S, Yang J, Zhai M et al (2020) Thermal stability of YSZ thick thermal barrier coatings deposited by suspension and atmospheric plasma spraying. Curr Comput-Aided Drug Des 10(11):984. https://doi.org/10.3390/cryst10110984
72. Rudolphi M, Galetz MC, Schütze M (2021) Mechanical stability diagrams for thermal barrier coating systems. J Therm Spray Technol 30:694–707. https://doi.org/10.1007/s11666-021-01163-5
73. Andreiko IM, Kulyk VV, Ostash OP (2012) Resistance of steels of railroad wheels to corrosion-fatigue fracture. Mater Sci 47(5):608–612. https://doi.org/10.1007/s11003-012-9434-9
74. Sciazko A, Shimura T, Komatsu Y et al (2021) Ni-GDC and Ni-YSZ electrodes operated in solid oxide electrolysis and fuel cell modes. J Therm Sci Technol 16(1):JTST0013. https://doi.org/10.1299/jtst.2021jtst0013
75. Nykyforchyn H, Krechkovska H, Student O et al (2019) Feature of stress corrosion cracking of degraded gas pipeline steels. Procedia Struct Integrity 16:153–160. https://doi.org/10.1016/j.prostr.2019.07.035
76. Romaniv OM, Vasyliv BD (1998) Some features of formation of the structural strength of ceramic materials. Mater Sci 34(2):149–161. https://doi.org/10.1007/BF02355530
77. Efremenko VG, Chabak YG, Lekatou A et al (2016) High-temperature oxidation and decarburization of 14.55 wt pct Cr-cast iron in dry air atmosphere. Metall Mater Trans A 47A(2):1529–1543. https://doi.org/10.1007/s11661-016-3336-7
78. Buchaniec S, Sciazko A, Mozdzierz M et al (2019) A novel approach to the optimization of a solid oxide fuel cell anode using evolutionary algorithms. IEEE Access 7:34361–34372. https://doi.org/10.1109/ACCESS.2019.2904327
79. Romaniv OM, Zalite IV, Simin'kovych VM et al (1996) Effect of the concentration of zirconium dioxide on the fracture resistance of $Al_2O_3$-$ZrO_2$ ceramics. Mater Sci 31(5):588–594. https://doi.org/10.1007/BF00558793
80. Khajavi P, Hendriksen PV, Chevalier J et al (2020) Improving the fracture toughness of stabilized zirconia-based solid oxide cells fuel electrode supports: effects of type and concentration of stabilizer(s). J Eur Ceram Soc 40(15):5670–5682. https://doi.org/10.1016/j.jeurceramsoc.2020.05.042
81. Ivasyshyn AD, Vasyliv BD (2001) Effect of the size and form of specimens on the diagram of growth rates of fatigue cracks. Mater Sci 37(6):1002–1004. https://doi.org/10.1023/A:1015669913601
82. Vasyliv BD (2002) Initiation of a crack from the edge of a notch with oblique front in specimens of brittle materials. Mater Sci 38(5):724–728. https://doi.org/10.1023/A:1024222709514
83. Cook RF, Pharr GM (1990) Direct observation and analysis of indentation cracking in glasses and ceramics. J Am Ceram Soc 73(4):787–817. https://doi.org/10.1111/j.1151-2916.1990.tb05119.x
84. Ostash OP, Kulyk VV, Lenkovskiy TM et al (2018) Relationships between the fatigue crack growth resistance characteristics of a steel and the tread surface damage of railway wheel. Arch Mater Sci Eng 90(2):49–55. https://doi.org/10.5604/01.3001.0012.0662
85. Nastic A, Merati A, Bielawski M et al (2015) Instrumented and Vickers indentation for the characterization of stiffness, hardness and toughness of zirconia toughened $Al_2O_3$ and SiC armor. J Mater Sci Technol 31(8):773–783. https://doi.org/10.1016/j.jmst.2015.06.005
86. Duriagina Z, Kulyk V, Kovbasiuk T et al (2021) Synthesis of functional surface layers on stainless steels by laser alloying. Metals 11(3):434. https://doi.org/10.3390/met11030434
87. ASTM E 384-11 (2011) Standard test method for Knoop and Vickers hardness of materials, ASTM International. https://doi.org/10.1520/E0384-11
88. ASTM C 1327-03 (2003) Standard test method for Vickers indentation hardness of advanced ceramics, ASTM International. https://doi.org/10.1520/C1327-03

89. Lawn BR, Swain MV (1975) Microfracture beneath point indentations in brittle solids. J Mater Sci 10(1):113–122. https://doi.org/10.1007/BF00541038
90. Gogotsi GA, Dub SN, Lomonova EE et al (1995) Vickers and Knoop indentation behaviour of cubic and partially stabilized zirconia crystals. J Eur Ceram Soc 15(5):405–413. https://doi.org/10.1016/0955-2219(95)91431-M
91. Evans AG, Charles EA (1976) Fracture toughness determinations by indentation. J Am Ceram Soc 59(7–8):371–372. https://doi.org/10.1111/j.1151-2916.1976.tb10991.x
92. Grigoriev ON, Vinokurov VB, Mosina TV et al (2017) Kinetics of shrinkage, structurization, and the mechanical characteristics of zirconium boride sintered in the presence of activating additives. Powder Metall Met Ceram 55(11–12):676–688. https://doi.org/10.1007/s11106-017-9855-y
93. Anstis GR, Chantikul P, Lawn BR et al (1981) A critical evaluation of indentation techniques for measuring fracture toughness: I, Direct crack measurement. J Am Ceram Soc 64(9):533–538. https://doi.org/10.1111/j.1151-2916.1981.tb10320.x
94. Danilenko I, Glazunov F, Konstantinova T et al (2014) Effect of Ni/NiO particles on structure and crack propagation in zirconia based composites. Adv Mater Lett 5(8):465–471. https://doi.org/10.5185/amlett.2014.amwc1040II
95. Lawn BR, Evans AG, Marshall DB (1980) Elastic/plastic indentation damage in ceramics: the median/radial crack system. J Am Ceram Soc 63(9–10):574–581. https://doi.org/10.1111/j.1151-2916.1980.tb10768.x
96. Smyrnova-Zamkova MY, Ruban OK, Bykov OI et al (2021) The influence of the $ZrO_2$ solid solution amount on the physicochemical properties of $Al_2O_3$–$ZrO_2$–$Y_2O_3$–$CeO_2$ powders. Powder Metall Met Ceram 60(3–4):129–141. https://doi.org/10.1007/s11106-021-00222-4
97. Lankford J (1982) Indentation microfracture in the Palmqvist crack regime: implications for fracture toughness evaluation by the indentation method. J Mater Sci Lett 1(11):493–495. https://doi.org/10.1007/BF00721938
98. Vasyliv B, Kulyk V, Duriagina Z et al (2020) Estimation of the effect of redox treatment on microstructure and tendency to brittle fracture of anode materials of YSZ–NiO(Ni) system. Eastern-Eur J Enterprise Technol 108/6(12):67–77. https://doi.org/10.15587/1729-4061.2020.218291
99. Kulyk VV, Duriagina ZA, Vasyliv BD et al (2021) Effects of yttria content and sintering temperature on the microstructure and tendency to brittle fracture of yttria-stabilized zirconia. Arch Mater Sci Eng 109(2):65–79. https://doi.org/10.5604/01.3001.0015.2625
100. ASTM E 399-20a (2020) Standard test method for linear-elastic plane-strain fracture toughness of metallic materials, ASTM International. https://doi.org/10.1520/E0399-20A
101. ASTM C 1421-18 (2018) Standard test methods for determination of fracture toughness of advanced ceramics at ambient temperature, ASTM International. https://doi.org/10.1520/C1421-18
102. Kübier J (2002) Fracture toughness of ceramics using the SEVNB method: From a preliminary study to a standard test method. In: Salem J et al (eds) Fracture resistance testing of monolithic and composite brittle materials. ASTM International, pp 93–106. https://doi.org/10.1520/STP10473S
103. Akselrud LY, Grin (2014) WinCSD: software package for crystallographic calculations (Version 4). J Appl Crystallogr 47:803–805. https://doi.org/10.1107/S1600576714001058